Original Research Article

Prediction of radiologic outcome-optimized dose plans and post-treatment magnetic resonance images: A proof-of-concept study in breast cancer brain metastases treated with stereotactic radiosurgery

Shraddha Pandey [a,d], Tugce Kutuk [b], Mahmoud A. Abdalah [c], Olya Stringfield [c], Harshan Ravi [a], Matthew N. Mills [b], Jasmine A. Graham [b,e], Kujtim Latifi [b,e], Wilfrido A. Moreno [d], Kamran A. Ahmed [b,e], Natarajan Raghunand [a,e,*]

[a] Department of Cancer Physiology, Moffitt Cancer Center, Tampa, FL 33612, USA
[b] Department of Radiation Oncology, H. Lee Moffitt Cancer Center and Research Institute, Tampa, FL 33612, USA
[c] Quantitative Imaging Shared Service, H. Lee Moffitt Cancer Center and Research Institute, Tampa, FL 33612, USA
[d] Department of Electrical Engineering, University of South Florida, Tampa, FL 33612, USA
[e] Department of Oncologic Sciences, University of South Florida, Tampa, FL 33612, USA

A B S T R A C T

Background and purpose: Information in multiparametric Magnetic Resonance (mpMR) images is relatable to voxel-level tumor response to Radiation Treatment (RT). We have investigated a deep learning framework to predict (i) post-treatment mpMR images from pre-treatment mpMR images and the dose map ("forward models"), and, (ii) the RT dose map that will produce prescribed changes within the Gross Tumor Volume (GTV) on post-treatment mpMR images ("inverse model"), in Breast Cancer Metastases to the Brain (BCMB) treated with Stereotactic Radiosurgery (SRS).

Materials and methods: Local outcomes, planning computed tomography (CT) images, dose maps, and pre-treatment and post-treatment Apparent Diffusion Coefficient of water (ADC) maps, T1-weighted unenhanced (T1w) and contrast-enhanced (T1wCE), T2-weighted (T2w) and Fluid-Attenuated Inversion Recovery (FLAIR) mpMR images were curated from 39 BCMB patients. mpMR images were co-registered to the planning CT and intensity-calibrated. A 2D pix2pix architecture was used to train 5 forward models (ADC, T2w, FLAIR, T1w, T1wCE) and 1 inverse model on 1940 slices from 18 BCMB patients, and tested on 437 slices from another 9 BCMB patients.

Results: Root Mean Square Percent Error (RMSPE) within the GTV between predicted and ground-truth post-RT images for the 5 forward models, in 136 test slices containing GTV, were (mean ± SD) 0.12 ± 0.044 (ADC), 0.14 ± 0.066 (T2w), 0.08 ± 0.038 (T1w), 0.13 ± 0.058 (T1wCE), and 0.09 ± 0.056 (FLAIR). RMSPE within the GTV on the same 136 test slices, between the predicted and ground-truth dose maps, was 0.37 ± 0.20 for the inverse model.

Conclusions: A deep learning-based approach for radiologic outcome-optimized dose planning in SRS of BCMB has been demonstrated.

1. Introduction

Rates of Breast Cancer Metastases to the Brain (BCMB) are increasing with improved systemic control of metastatic breast cancer [1]. SRS and fractionated SRS (fSRS) represent the current standard treatment for patients with limited number of brain metastases, after surgery or as definitive treatment [2–5]. SRS and fSRS can lead to late toxicities, with radionecrosis (RN) being the most common. RN is a potentially devastating long-term side effect of SRS for brain metastases, with a reported incidence ranging from 6 % to 24 % [2,6–10]. Onset of RN is usually 3–12 months after SRS but can also occur later [10]. RN can cause seizures, cognitive deficits and other non-specific symptoms, depending on the affected area, or it can be asymptomatic and diagnosed on serial follow-up imaging. Currently, the radiation dose prescribed to a tumor

---

by the radiation oncologist is based on nationally accepted standards and evidence from clinical trials [11–13]. Intra-tumor and inter-tumor biologic variations produce heterogeneities in sensitivity to radiation [14], and there is a need for automated tools to aid the radiation oncologist in prescribing optimal dose distributions to achieve maximal control of spatially heterogenous tumors while averting toxicities such as RN.

Multiparametric Magnetic Resonance Images (mpMRIs) contain information that is mechanistically relatable to voxel-level tumor response to therapies. For example, Diffusion-Weighted MRI (DW-MRI) is sensitive to changes in viable cellularity in the tumor [15,16]. Microbleeds and metal scavenging in melanoma brain metastases, particularly following Radiation Treatment (RT), can be visualized on Susceptibility-Weighted Imaging [17]. Perfusion imaging by Dynamic Susceptibility Contrast MRI is useful for differentiating recurrent brain metastases from radiation treatment-related changes [18]. Dynamic Contrast-Enhanced MRI (DCE-MRI) provides quantitative voxelwise measures of tumor perfusion, vascularity, and microvascular permeability that are responsive to changes in brain metastases following SRS [19,20]. The value of radiation dose boost to tumor regions that are hypercellular (identified on pre-RT DW-MRI) with high perfusion (identified on pre-RT DCE-MRI) has been investigated, on the hypothesis that hypercellular-hyperperfused regions have a greater likelihood of tumor recurrence post-radiation [21–24].

We have considered the feasibility and utility of deep learning models to inform dose painting for prescribed radiologic outcomes. In this proof-of-concept study in BCMB patients treated with SRS we report preliminary "forward models" for predicting post-treatment mpMRIs from co-registered pre-treatment mpMRIs and the delivered RT dose map, and a preliminary "inverse model" for predicting the RT dose map that will yield prescribed values in treated voxels on post-treatment mpMRIs. We have investigated post-RT vs. pre-RT changes in calibrated intensity within the treated volume that are associated with local tumor control without toxicity. Such post-RT mpMRI intensity criteria could serve as targets for radiologic outcome-optimized RT dose planning using the inverse and forward models, as envisioned in Fig. 1.

2. Materials and methods

2.1. Patient data

In this retrospective IRB-approved study (PRO00023399), planning CT images and associated RT dose maps, Apparent Diffusion Coefficient of water (ADC) maps, T1-weighted unenhanced (T1w) and contrast-enhanced (T1wCE), T2-weighted (T2w) and Fluid-Attenuated Inversion Recovery (FLAIR) mpMR images acquired pre-RT (3–33 days), post-RT (12–143 days), at local recurrence if applicable (54–831 days), and at diagnosis of RN if applicable (44–1088 days), in 39 BCMB patients were curated from our Radiology and Radiation Oncology databases [25]. Brain metastases were assessed on pre-radiation MRI reconstructed with 1 mm slices and fused with CT simulation imaging. The GTV was expanded uniformly by 1–2 mm to create the Planning Target Volume (PTV). Dose (range 15–30 Gy, mean 21 Gy) and fractionation (1–5 fractions) were based on physician preference. Doses were prescribed to ensure coverage of ≥ 95 % of the PTV with the prescription dose. Plans were generated using Brainlab software. Treatments were initiated within 2 weeks of simulation CT using multiple dynamic conformal arcs or Intensity Modulated Radiotherapy (IMRT), with image guidance by the Brainlab ExacTrac positioning system. Data from 27 patients with complete and artifact-free mpMR image sets, and matched spin-echo acquisitions of T1w and T1wCE images at pre-RT and post-RT, were randomly split into training (18 patients) and test (9 patients) cohorts. Dose maps from multiple fractions, where applicable, were summed and used in the following analyses.

2.2. Image Pre-Processing

mpMRIs from all scan dates were resampled and co-registered with the planning CT using MIRADA-RTx (Mirada Medical, Denver, CO, USA). Voxel intensities on skull-stripped, co-registered T2w, FLAIR, T1w and T1wCE images were calibrated [26] as detailed in Supplementary Materials. Intensity-calibrated voxels on co-registered mpMRI were assigned to objectively-defined tissue types for visual quality check of spatial registration and intensity-calibration (Supplementary Figs. S1–S5).
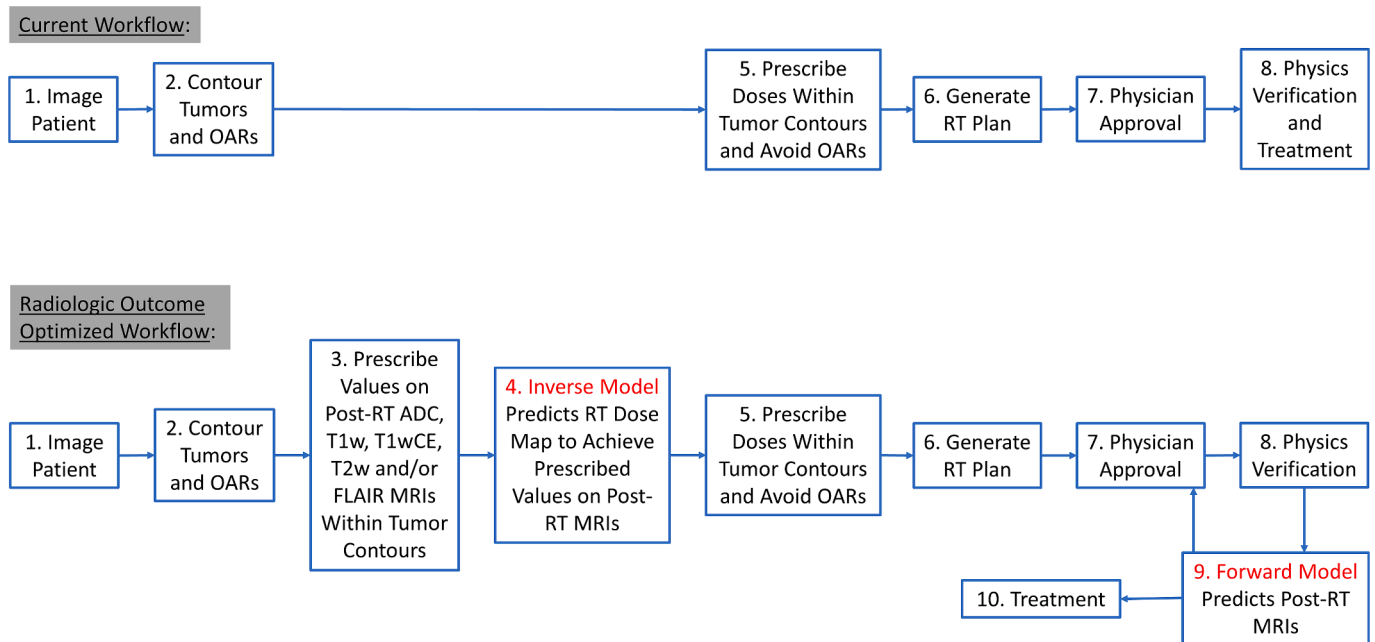
Fig. 1. Envisioned utility of the proposed forward and inverse models in a workflow for mpMRI outcome-optimized RT dose planning. ADC: Apparent Diffusion Coefficient of water; T1w: calibrated unenhanced T1-weighted MRI intensity; T1wCE: calibrated contrast-enhanced T1-weighted MRI intensity; T2w: calibrated T2-weighted MRI intensity; FLAIR: calibrated Fluid Attenuated Inversion Recovery MRI intensity; RT: radiation treatment; OARs: organs at risk.

2.3. RT dose vs. mpMRI response

Voxelwise subtraction of calibrated post-RT and pre-RT whole brain mpMR images was performed to calculate ΔADC, ΔT2w, ΔFLAIR, ΔT1w and ΔT1wCE. Voxelwise change in enhancement (ΔΔT1w) was computed as $(T1wCE - T1w)_{post-RT}$ minus $(T1wCE - T1w)_{pre-RT}$. Voxels in these 6 subtraction images were binned per patient by total RT dose received, and the Mean of Means ± Standard Error of Means (S.E.M) over all patients visualized as RT dose vs. mpMRI response plots.

2.4. Lesion outcomes vs. mpMRI response

Responding vs. locally-recurrent vs. RN lesions were compared by mean calibrated intensity changes (ΔADC, ΔT2w, ΔFLAIR, ΔT1w, ΔT1wCE) within the GTV.

2.5. Deep learning

We extended the one-input-one-output 2D pix2pix architecture published by Isola et al. [27] to *n*-input-one-output, with 54,418,177 trainable weights, for training the forward and inverse models (details in Supplementary Materials sections 3.1 and 3.2). pix2pix is a type of conditional generative adversarial network (GAN) with a UNET-based [28] generator and a patchGAN discriminator [27]. The adversarial loss is combined with the L1 loss into a composite loss function that is used to update the generator [27]. Fig. 2(a) depicts how a Forward Model was trained to predict a given post-RT mpMRI type, in this case

ADC, from all 5 pre-RT mpMRIs and the RT dose map. Fig. 2(b) depicts how the inverse model was trained to predict the RT dose map corresponding to 5 pre-RT and 5 target/desired post-RT mpMRIs. The models were optimized on training data using the following numbers of iterations: T1wCE – 225, T2w – 200, T1w – 150, FLAIR – 175, ADC – 125, and, inverse model – 150. We also optimized the learning rate of the models. For the generator, we tuned the weighted sum of adversarial loss (BCE) and L1 loss, and found a ratio of 1:100 to be optimal on the training data [27]. For the discriminator, the standard deviation of the exponentially decaying gaussian noise added to the real and fake inputs was optimized on training data.

2.6. Evaluation of forward and inverse models

The 5 forward models (to predict post-RT ADC, T2w, FLAIR, T1w, and T1wCE) and 1 inverse model were trained on 1940 slices from 18 BCMB patients and tested on 437 held-out slices (136 slices containing GTV) from another 9 BCMB patients.

Forward models were provided pre-RT ADC, T2w, FLAIR, T1w, and T1wCE images of a given slice, and the RT dose map delivered to that slice, with the model output being the predicted post-RT image (ADC, T2w, FLAIR, T1w or T1wCE) of that slice. This predicted post-RT image was compared to the corresponding ground-truth post-RT image on the basis of Root Mean Square Percent Error (RMSPE).

We envision the inverse model being used to predict the dose map that will yield prescribed changes within the GTV on post-RT ADC, T2w, FLAIR, T1w, and T1wCE (Fig. 1). To test the inverse model we provided
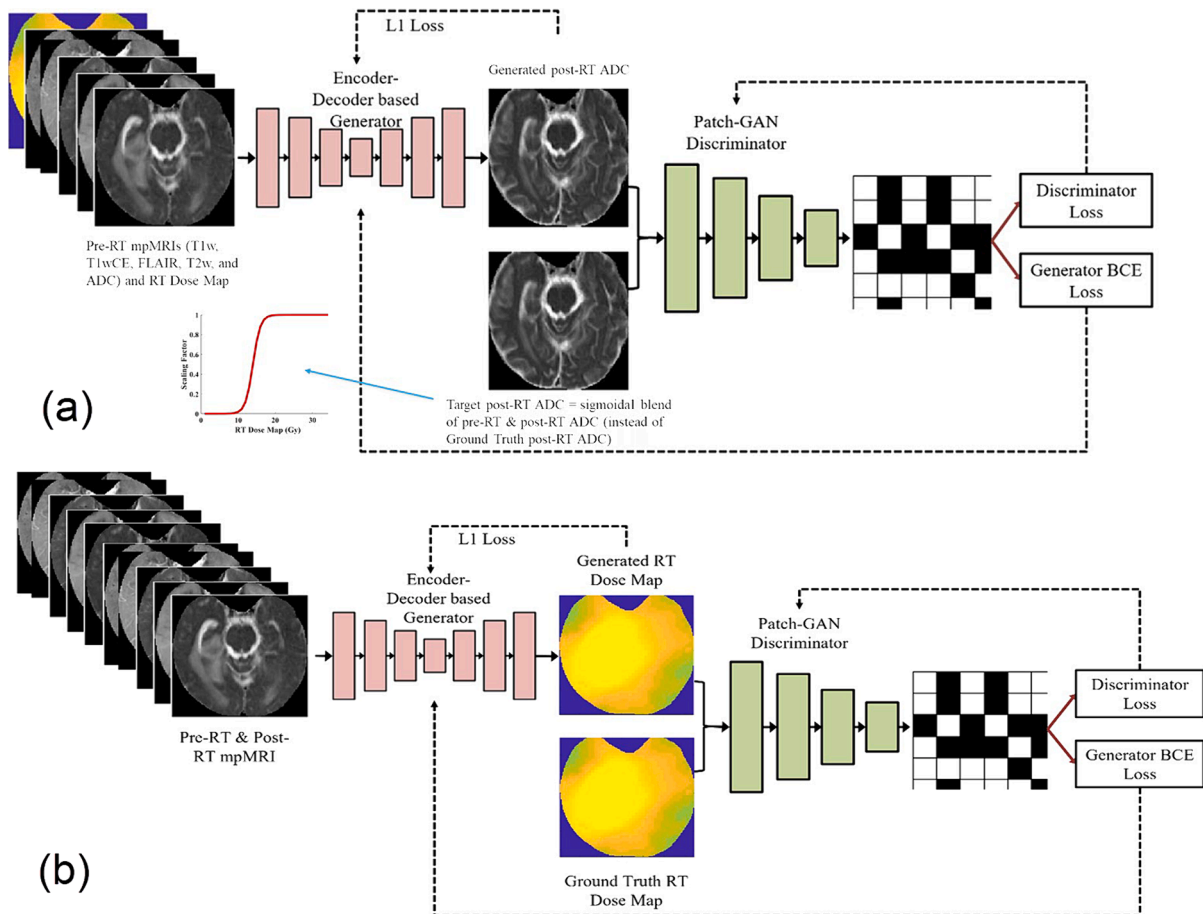
Fig. 2. 2D pix2pix model training framework. (a) Forward Model: The inputs to the forward model were the co-registered RT dose map and pre-RT mpMRIs, while the target was a sigmoidal dose-dependent blend (inset) of the ground truth pre-RT and post-RT image of a given type (ADC in this example). (b) Inverse Model: The input images to the inverse model were the 5 types of co-registered pre-RT mpMRIs and corresponding 5 types of post-RT mpMRIs, while the target was the ground truth RT dose map delivered to the slice.

the following inputs: pre-RT ADC, T2w, FLAIR, T1w, and T1wCE images of a given slice, and "desired" post-RT ADC, T2w, FLAIR, T1w, and T1wCE images of the same slice that were identical to the corresponding pre-RT mpMRIs except that pixel values within the GTV were replaced with corresponding ground truth post-RT values. The model output was a dose map predicted to produce these changes within the GTV on ADC, T2w, FLAIR, T1w, and T1wCE, which was compared to the actual dose map delivered to that slice using RMSPE.

We simulated inverse model predictions of RT dose distributions required to produce four hypothetical cases of post-RT changes within the GTV: either moderate (1500 μm²/s) or high (3000 μm²/s) desired post-RT ADC in the GTV, and either partial suppression of contrast-enhancement (desired post-RT T1wCE = voxelwise average of pre-RT T1w and pre-RT T1wCE) or complete suppression of contrast-enhancement within the GTV (desired post-RT T1wCE = true pre-RT T1w).

2.7. Statistical analysis

ΔADC, ΔT2w, ΔFLAIR, ΔT1w and ΔT1wCE within the GTVs of 10 responding, 14 recurrent, & 10 RN BCMB lesions treated with SRS were compared using unpaired Student's t-test (significance threshold p < 0.05). RMSPE between calibrated-normalized-scaled ground truth (I^{GT}) and predicted voxel intensities (I^{Pred}) was calculated as:

$$RMSPE = \left(\sqrt{\frac{\left(\sum_{j=1}^{V} \left(I_j^{GT} - I_j^{Pred}\right)^2\right)}{V}} \right) / R \qquad (1)$$

where R is the expected post-scaling intensity range (-1 to $+1 = 2$), and V is the number of voxels in a GTV.

3. Results

3.1. RT dose vs. mpMRI response

mpMRI response to RT was analyzed in 39 subjects, though some images were dropped due to presence of artifacts (ADC) or because T1w and T1wCE were not acquired with matched SE or GRE sequences (Fig. 3). ADC response is negligible below a dose of ≈23 Gy, above which post-RT ADC increases relative to pre-RT ADC (Fig. 3a).

Calibrated post-RT FLAIR intensity tends to decrease relative to pre-RT values with increasing dose above ≈10 Gy (Fig. 3b), and calibrated post-RT T2w intensity decreases relative to pre-RT intensity at doses above ≈18 Gy (Fig. 3c), though these trends are noisy at the highest doses due to a smaller number of voxels that received those doses. Unenhanced T1w intensity is largely unchanged at doses below ≈28 Gy, above which calibrated post-RT T1w intensity tends to increase relative to pre-RT intensity (Fig. 3d). Calibrated post-RT T1wCE intensity appears to decrease relative to pre-RT T1wCE with increasing dose above ≈20 Gy (Fig. 3e); subtraction of the confounding increase in post-RT T1w relative to pre-RT T1w with dose makes this trend more apparent (Fig. 3f).

3.2. Lesion outcomes vs. mpMRI response

We have compared mean ΔADC, ΔFLAIR, ΔT2w, ΔT1w, and ΔT1wCE intensity changes within the GTV between 10 responding, 14 recurrent, and 10 RN lesions in 28 BCMB patients treated with SRS (Fig. 4). ΔT1wCE was positive in responding lesions and negative in RN lesions (p < 0.04). ΔFLAIR was positive in responding lesions, negative in locally-recurrent lesions, and close to zero in RN lesions, though these differences did not reach statistical significance. ΔADC was higher in responding lesions compared with locally-recurrent and RN lesions, though this difference also did not reach statistical significance. ΔT1 and ΔT2 tended positive in RN lesions and negative in recurrent lesions, though these trends were not statistically significant (Fig. 4).

3.3. Forward model test results

The 5 forward models were used to predict post-RT mpMRIs from the pre-RT mpMRIs and the delivered RT dose distribution. In the test patient in Fig. 5(a), the forward model predicts a post-RT decrease in FLAIR intensity within the GTV, in significant agreement with the ground truth post-RT FLAIR. No enhancement within the GTV is predicted on post-RT T1wCE by the forward model, in agreement with ground truth post-RT T1wCE. Agreement between forward model-predicted post-RT and ground truth post-RT is partial on ADC, T2w and FLAIR. In the test patient in Fig. 5(b), there is moderate agreement between forward model-predicted post-RT and ground truth post-RT images on all 5 scan types. RMSPE within the GTV between the predicted post-RT images and the ground-truth post-RT images, in 136 test slices that contained GTV, were 0.12 ± 0.044 (ADC), 0.14 ± 0.066 (T2w), 0.08 ± 0.038 (T1w), 0.13 ± 0.058 (T1wCE), and 0.09 ± 0.056
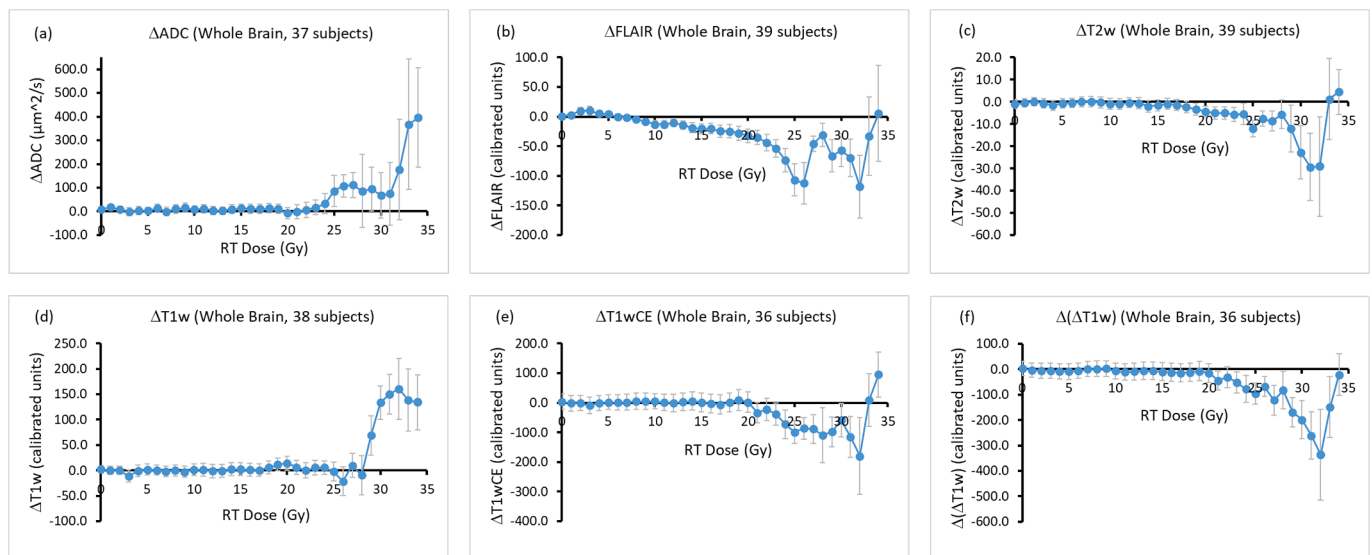
Fig. 3. The y-axes plot the mean of means ± S.E.M of the voxelwise change (post-RT − pre-RT) in mpMRI intensity across all subjects at each dose level (x-axes) over the whole brain: (a) ΔADC vs. RT dose, (b) ΔFLAIR vs. RT dose, (c) ΔT2w vs. RT dose, (d) ΔT1w vs. RT dose, (e) ΔT1wCE vs. RT dose, (f) ΔΔT1w vs. RT dose.
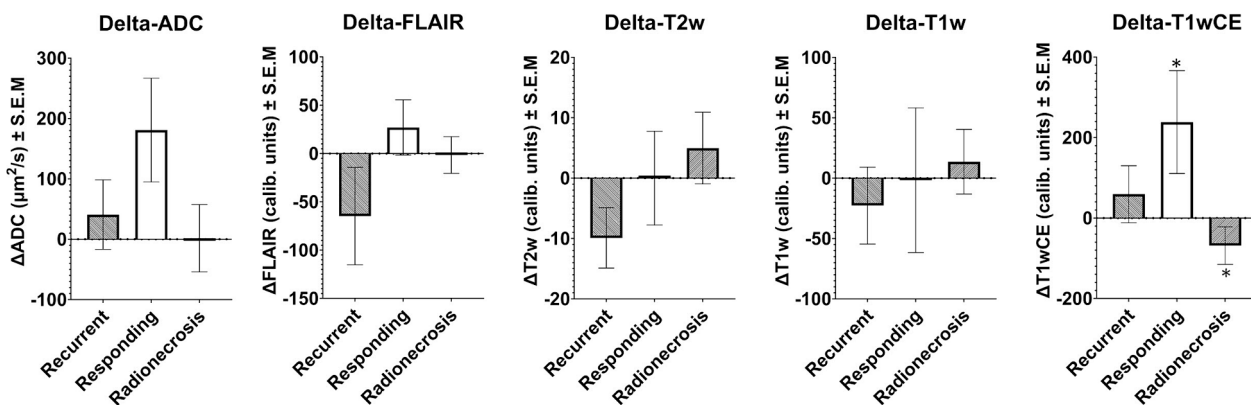
Fig. 4. post-RT minus pre-RT changes on ADC maps and calibrated FLAIR, T2w, T1w, and T1wCE MRI within the GTVs of 10 responding, 14 recurrent, & 10 RN lesions in 28 BCMB patients treated with SRS. * indicates a significant difference ($p < 0.04$).
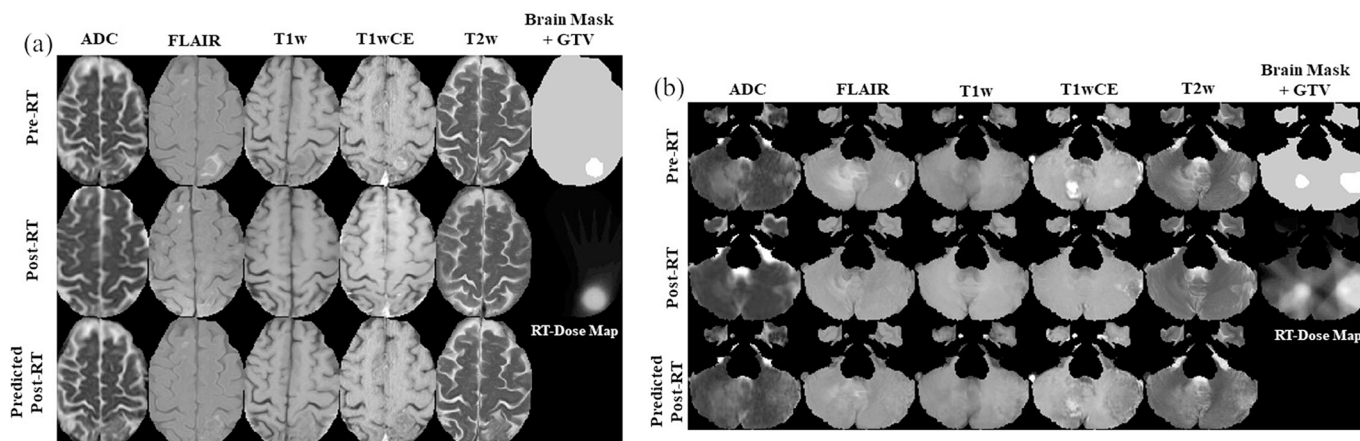

Fig. 5. Example test results of the Forward Models in two patients. In both panels the top row shows the pre-RT mpMRIs of a test slice, the middle row shows the co-registered ground truth post-RT mpMRIs of the same slice, and the bottom row shows the post-RT mpMRIs predicted by the 5 forward models for the delivered RT dose map that is also shown in the middle row. Brain masks and GTV masks are shown on the top row for visual reference, but were not used as model inputs.

(FLAIR). Results for individual test slices are listed in Supplementary Table 2.

3.4. Inverse model test results

The inverse model was used to predict RT dose distributions that would produce the observed post-RT mpMRI voxel intensities within the GTV. In the test patients shown in Fig. 6, the inverse model predicts dose distributions within the GTV that bear qualitative similarity to the ground truth dose distributions actually delivered to these slices. However, it also predicts non-zero doses outside the GTV even though the target/desired post-RT mpMRIs were created to differ from pre-RT mpMRIs only inside the GTV. Additional examples from each of the 9 test subjects are presented in Supplementary Fig. S6(a)-S6(i). RMSPE within the GTV between the predicted RT dose maps and the ground-truth dose maps was 0.37 ± 0.20; results for all 136 test slices that contained GTV are listed in Supplementary Table 2. In simulations, the inverse model predicts that higher doses to tumor would be required to produce higher post-RT tumor ADC and/or lower post-RT contrast enhancement on T1wCE (Supplementary Fig. 7).

4. Discussion

Rule-based, atlas-based and prior-knowledge based methods have been reported for planning the delivery of a prescribed radiation dose to targeted tumors while sparing organs-at-risk (OARs), but such automated treatment planning solutions do not provide voxel-level predictions of RT dose that are optimal for specific outcomes [29–33]. Dose boosting to a sub-volume within the target, and Dose Painting by Numbers (DPbN), are two broad approaches for prescribing non-uniform RT dose distributions to target heterogeneous tumors [34–37]. DPbN requires knowledge of a prescription function that mathematically transforms specific values of an imaging variable into the corresponding optimum dose values [35]. In the absence of such a known prescription function, some groups have assumed a linear relationship between voxel intensities on radiologic images and the dose to be prescribed [38,39], while others have investigated redistribution of the Maximum Tolerated Dose (MTD) according to ^{18}F-Fluorodeoxyglucose (FDG) uptake on PET/CT in Head and Neck Squamous Cell Carcinoma (HNSCC) [40–42]. Information from pre-RT ADC maps and multi-tracer PET images has been combined to compute tumor control probability functions that inform focal dose-escalation to prostate tumor sub-volumes [43,44]. In HNSCC patients treated with standard chemoradiation, the logarithm of relative change in FDG-PET SUV on serial FDG-PET/CT images was modeled as a linear random function of treatment dose for doses below 40 Gy, normalized using the in vitro tumor survival fraction at 2 Gy, and combined with voxelwise baseline FDG SUV to compute a dose prescription function to guide treatment dose adaptation in a subsequent fraction [45,46]. Recently, in a study of oropharyngeal cancer patients treated with IMRT, models to predict post-RT FDG-PET images from pre-RT FDG-PET images and the RT dose map have been described [47,48].
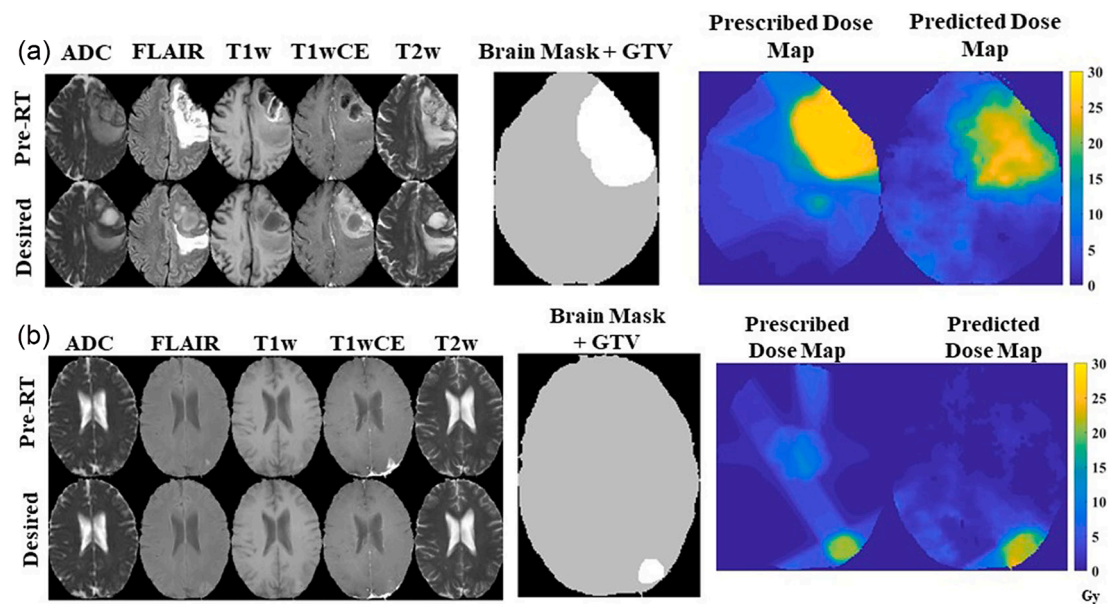
Fig. 6. Two examples of test results from the Inverse Model. The inputs to the trained inverse models were: (i) 5 calibrated pre-RT mpMRI images as shown in the top row of each panel (ADC map and calibrated FLAIR, T2w, T1w and T1wCE images), and, (ii) 5 "desired" post-RT mpMRI images as shown in the bottom rows of each panel that were identical to the pre-RT mpMRIs except that pixel values within the GTV were replaced with corresponding values from co-registered ground truth post-RT mpMRIs. In each case the inverse model predicts an RT dose map that will produce these target post-RT mpMRIs, to be compared with the actual dose map administered to this slice. Brain masks and GTV masks are shown for visual reference but were not used as model inputs.

We have proposed an inverse model that will take pre-RT mpMRIs as inputs to predict the RT dose distribution required to achieve prescribed mpMRI outcomes within the GTV. We envision that this predicted radiologic outcome-optimized dose distribution will inform the physician's dose prescription (Fig. 1, step 5), following which treatment is planned, approved by the physician, sent for physics QA, post-RT outcomes to this plan predicted using the forward model, with iterative fine-tuning of the plan by the physician if necessary, before the patient is treated (Fig. 1).

We observed increasing ΔADC, suggesting cell death [15,16], with increasing RT dose (Fig. 3(a)). Net change in contrast-enhancement ΔΔT1w trended negative with increasing RT dose (Fig. 3(f)), consistent with RANO-BM criteria [49–51]. ΔFLAIR and ΔT2w also trended negative with increasing dose (Fig. 3(b)-(c)), suggesting a decrease in vasogenic edema with RT. There is an apparent change in trend above 32 Gy on ΔFLAIR, ΔT2w, ΔT1wCE and ΔΔT1w, though not many voxels received these doses. Interestingly, ΔT1w increases at higher doses, suggesting the formation of hemorrhagic and/or proteinaceous products (Fig. 3(d)). This underlying change on ΔT1w may explain the counter-intuitive finding that ΔT1wCE is positive in responding lesions and negative in RN lesions (Fig. 4). A multivariable analysis of mpMRI changes corresponding to local response, recurrence and RN, on a larger and more diverse dataset, is required for identifying statistically robust criteria on post-RT and/or ΔmpMRIs corresponding to local response without RN, to inform step 3 in Fig. 1.

The 5 forward models achieved RMSPE values of 0.08–0.14 (8–14 %) inside the GTV. The inverse model predictions qualitatively resemble the dose distributions delivered to the GTV (Supplementary Fig. S6(a)-(i)) though voxelwise similarity within the GTV was heterogeneous over all test slices (RMSPE 0.37 ± 0.2 (37 ± 20 %), Supplementary Table 2). The resection cavity in Test Patient #4 (Supplementary Fig. S6d) received a high dose but, unsurprisingly, did not change significantly post-RT vs. pre-RT; the inverse model rationally predicts that a lower dose would have achieved this radiologic outcome, leading to high RMSPE (Supplementary Table 2). The mpMRI response to low RT doses is small (Fig. 3), which may explain the higher RMSPE of 0.74 in Test Patient #5 who received a relatively low dose (Supplementary Fig. S6e

and Supplementary Table 2). Increase in ADC [15,16] and decrease in contrast enhancement [49–51] are associated with tumor response to cytotoxic therapies. The inverse model predicts that a progressively higher RT dose distribution to the GTV is required for hypothetical moderate tumor control (moderate ADC and partial suppression of contrast enhancement) through hypothetical aggressive tumor control (high ADC and no contrast enhancement), indicating that the model has "learned" physiologically meaningful relationships between RT dose and post-RT changes on mpMRI (Supplementary Fig. 7).

The forward models predict voxel intensities similar to the pre-RT images in low dose regions, a limitation stemming from using blended target post-RT images to train the forward models (Fig. 2a inset, details in Supplementary Materials). The inverse model predicts non-zero doses outside the GTV, and a spatial shift between the GTV and predicted high dose regions is observable in some cases. Another limitation is that we trained our models on total dose rather than biologically equivalent dose, given the limited number of local recurrences in our dataset, which misdirected model training at high doses (multiple fractions). In future work we will train our models on a greater number and diversity of samples, explicitly accounting for the number of fractions and the time gaps between MRIs and the start/end of RT. As with DPbN [38,41,52], new treatment planning processes may need to be developed to incorporate the forward and inverse models into the clinical workflow. Ultimately, we anticipate that these novel tools will enable optimal targeting of BCMB while avoiding toxic side-effects like radionecrosis.

CRediT authorship contribution statement

Shraddha Pandey: Formal analysis, Investigation, Methodology, Software, Validation, Visualization, Writing – original draft, Writing – review & editing. **Tugce Kutuk:** Data curation, Methodology, Formal analysis, Writing – review & editing. **Mahmoud A. Abdalah:** Data curation, Formal analysis, Software, Writing – review & editing. **Olya Stringfield:** Data curation, Formal analysis, Software, Writing – review & editing. **Harshan Ravi:** Methodology, Software, Writing – review & editing. **Matthew N. Mills:** Data curation, Writing – review & editing. **Jasmine A. Graham:** Data curation, Methodology, Writing – review &

editing. **Kujtim Latifi:** Data curation, Methodology, Writing – review & editing. **Wilfrido A. Moreno:** Supervision, Writing – review & editing. **Kamran A. Ahmed:** Data curation, Funding acquisition, Investigation, Methodology, Project administration, Resources, Supervision, Validation, Writing – review & editing. **Natarajan Raghunand:** Conceptualization, Data curation, Formal analysis, Funding acquisition, Investigation, Methodology, Project administration, Resources, Software, Supervision, Validation, Visualization, Writing – original draft, Writing – review & editing.

Declaration of competing interest

The authors declare that they have no known competing financial interests or personal relationships that could have appeared to influence the work reported in this paper.

Acknowledgements

Code sharing statement

Python 3.9 code for the "*n* input, one output" variant of pix2pix for model training and testing are available from the corresponding author on request.

Appendix A. Supplementary data

Supplementary data to this article can be found online at https://doi.org/10.1016/j.phro.2024.100602.

References

[1] Mills MN, Figura NB, Arrington JA, Yu HM, Etame AB, Vogelbaum MA, et al. Management of brain metastases in breast cancer: a review of current practices and emerging treatments. Breast Cancer Res Treat 2020;180:279–300.

[2] Calderon B, Vazquez L, Belkacemi M, Pourel N. Stereotactic radiotherapy for brain metastases: predictive factors of radionecrosis. Eur J Med Res 2023;28:233.

[3] Yamamoto M, Serizawa T, Shuto T, Akabane A, Higuchi Y, Kawagishi J, et al. Stereotactic radiosurgery for patients with multiple brain metastases (JLGK0901): a multi-institutional prospective observational study. LancetOncol 2014;15:387–95.

[4] Brown PD, Jaeckle K, Ballman KV, Farace E, Cerhan JH, Anderson SK, et al. Effect of Radiosurgery Alone vs Radiosurgery With Whole Brain Radiation Therapy on Cognitive Function in Patients With 1 to 3 Brain Metastases: A Randomized Clinical Trial. JAMA 2016;316:401–9.

[5] Brown PD, Ballman KV, Cerhan JH, Anderson SK, Carrero XW, Whitton AC, et al. Postoperative stereotactic radiosurgery compared with whole brain radiotherapy for resected metastatic brain disease (NCCTG N107C/CEC·3): a multicentre, randomised, controlled, phase 3 trial. LancetOncol 2017;18:1049–60.

[6] Minniti G, Clarke E, Lanzetta G, Osti MF, Trasimeni G, Bozzao A, et al. Stereotactic radiosurgery for brain metastases: analysis of outcome and risk of brain radionecrosis. Radiat Oncol 2011;6:48.

[7] Alomari A, Rauch PJ, Orsaria M, Minja FJ, Chiang VL, Vortmeyer AO. Radiologic and histologic consequences of radiosurgery for brain tumors. J Neuro-Oncol 2014;117:33–42.

[8] Sneed PK, Mendez J, Vemer-van den Hoek JG, Seymour ZA, Ma L, Molinaro AM, et al. Adverse radiation effect after stereotactic radiosurgery for brain metastases: incidence, time course, and risk factors. J Neurosurg 2015;123:373–86.

[9] Le Rhun E, Dhermain F, Vogin G, Reyns N, Metellus P. Radionecrosis after stereotactic radiotherapy for brain metastases. Expert Rev Neurother 2016;16:903–14.

[10] Lupattelli M, Alì E, Ingrosso G, Saldi S, Fulcheri C, Borghesi S, et al. Stereotactic Radiotherapy for Brain Metastases: Imaging Tools and Dosimetric Predictive Factors for Radionecrosis. J Pers Med 2020:10.

[11] Huynh E, Hosny A, Guthier C, Bitterman DS, Petit SF, Haas-Kogan DA, et al. Artificial intelligence in radiation oncology. Nat Rev Clin Oncol 2020;17:771–81.

[12] Vogelbaum MA, Brown PD, Messersmith H, Brastianos PK, Burri S, Cahill D, et al. Treatment for Brain Metastases: ASCO-SNO-ASTRO Guideline. J Clin Oncol 2022;40:492–516.

[13] Shaw E, Scott C, Souhami L, Dinapoli R, Kline R, Loeffler J, et al. Single dose radiosurgical treatment of recurrent previously irradiated primary brain tumors and brain metastases: final report of RTOG protocol 90–05. Int J Rad Oncol Biol Phys 2000;47:291–8.

[14] Ahmed KA, Berglund AE, Welsh EA, Naghavi AO, Kim Y, Yu M, et al. The radiosensitivity of brain metastases based upon primary histology utilizing a multigene index of tumor radiosensitivity. Neuro-Oncol 2017;19:1145–6.

[15] Afaq A, Andreou A, Koh DM. Diffusion-weighted magnetic resonance imaging for tumour response assessment: why, when and how? Cancer Imaging 2010;10 Spec no A:S179–S88.

[16] Galbán CJ, Hoff BA, Chenevert TL, Ross BD. Diffusion MRI in early cancer therapeutic response assessment. NMR Biomed. 2017;30:10.1002/nbm.3458.

[17] Schwarz D, Niederle T, Münch P, Hielscher T, Hassel JC, Schlemmer HP, et al. Susceptibility-weighted imaging in malignant melanoma brain metastasis. J Magn Reson Imaging 2019;50:1251–9.

[18] Kwee RM, Kwee TC. Dynamic susceptibility MR perfusion in diagnosing recurrent brain metastases after radiotherapy: A systematic review and meta-analysis. J Magn Reson Imaging 2020;51:524–34.

[19] Taunk NK, Oh JH, Shukla-Dave A, Beal K, Vachha B, Holodny A, et al. Early posttreatment assessment of MRI perfusion biomarkers can predict long-term response of lung cancer brain metastases to stereotactic radiosurgery. Neuro-Oncol 2017;20:567–75.

[20] Shah AD, Shridhar Konar A, Paudyal R, Oh JH, LoCastro E, Nuñez DA, et al. Diffusion and Perfusion MRI Predicts Response Preceding and Shortly After Radiosurgery to Brain Metastases: A Pilot Study. J Neuroimaging 2021;31:317–23.

[21] Kim MM, Parmar HA, Aryal MP, Mayo CS, Balter JM, Lawrence TS, et al. Developing a Pipeline for Multiparametric MRI-Guided Radiation Therapy: Initial Results from a Phase II Clinical Trial in Newly Diagnosed Glioblastoma. Tomography 2019;5:118–26.

[22] Kim MM, Sun Y, Aryal MP, Parmar HA, Piert M, Rosen B, et al. A Phase 2 Study of Dose-intensified Chemoradiation Using Biologically Based Target Volume Definition in Patients With Newly Diagnosed Glioblastoma. Int J Radiat Oncol Biol Phys 2021;110:792–803.

[23] Kim MM, Aryal MP, Sun Y, Parmar HA, Li P, Schipper M, et al. Response assessment during chemoradiation using a hypercellular/hyperperfused imaging phenotype predicts survival in patients with newly diagnosed glioblastoma. Neuro-Oncol 2021;23:1537–46.

[24] Mierzwa ML, Aryal M, Lee C, Schipper M, VanTil M, Morales K, et al. Randomized Phase II Study of Physiologic MRI-Directed Adaptive Radiation Boost in Poor Prognosis Head and Neck Cancer. Clin Can Res 2022;28:5049–57.

[25] Mills MN, Thawani C, Figura NB, Oliver DE, Soyano AE, Etame A, et al. Breast cancer subtype predicts clinical outcomes after stereotactic radiation for brain metastases. J Neuro-Oncol 2021;152:591–601.

[26] Stringfield O, Arrington JA, Johnston SK, Rognin NG, Peeri NC, Balagurunathan Y, et al. Multiparameter MRI Predictors of Long-Term Survival in Glioblastoma Multiforme. Tomography 2019;5:135–44.

[27] Isola P, Zhu JY, Zhou T, Efros AA. Image-to-Image Translation with Conditional Adversarial Networks. 2017 IEEE Conference on Computer Vision and Pattern Recognition (CVPR)2017. p. 5967-76.

[28] Ronneberger O, Fischer P, Brox T. U-Net: Convolutional Networks for Biomedical Image Segmentation. In: Navab N, Hornegger J, Wells WM, Frangi AF, editors. Medical Image Computing and Computer-Assisted Intervention – MICCAI 2015. Cham: Springer International Publishing; 2015. p. 234–41.

[29] Nguyen D, Long T, Jia X, Lu W, Gu X, Iqbal Z, et al. A feasibility study for predicting optimal radiation therapy dose distributions of prostate cancer patients from patient anatomy using deep learning. Sci Rep 2019;9:1076.

[30] Ma M, M KB, Vasudevan V, Xing L, Yang Y. Dose distribution prediction in isodose feature-preserving voxelization domain using deep convolutional neural network. Med Phys 2019;46:2978–87.

[31] Ahn SH, Kim E, Kim C, Cheon W, Kim M, Lee SB, et al. Deep learning method for prediction of patient-specific dose distribution in breast cancer. Radiat Oncol. 2021;16:154- (13 pages).

[32] Murakami Y, Magome T, Matsumoto K, Sato T, Yoshioka Y, Oguchi M. Fully automated dose prediction using generative adversarial networks in prostate cancer patients. PLoS ONE 2020;15:e0232697.

[33] Meerbothe M. A physics guided neural network approach for dose prediction in automated radiation therapy treatment planning [Master of science]. Delft University of Technology; 2021.

[34] Ling CC, Humm J, Larson S, Amols H, Fuks Z, Leibel S, et al. Towards multidimensional radiotherapy (MD-CRT): biological imaging and biological conformality. Int J Radiat Oncol Biol Phys 2000;47:551–60.

[35] Bentzen SM. Theragnostic imaging for radiation oncology: dose-painting by numbers. LancetOncol 2005;6:112–7.

[36] Bentzen SM, Gregoire V. Molecular Imaging-Based Dose Painting: A Novel Paradigm for Radiation Therapy Prescription. Semin Radiat Oncol 2011;21:101–10.

[37] Grégoire V, Thorwarth D, Lee JA. Molecular Imaging-Guided Radiotherapy for the Treatment of Head-and-Neck Squamous Cell Carcinoma: Does it Fulfill the Promises? Semin Radiat Oncol 2018;28:35–45.

[38] Arnesen MR, Knudtsen IS, Rekstad BL, Eilertsen K, Dale E, Bruheim K, et al. Dose painting by numbers in a standard treatment planning system using inverted dose prescription maps. Acta Oncol 2015;54:1607–13.

[39] Brighi C, Keall PJ, Holloway LC, Walker A, Whelan B, de Witt Hamer PC, et al. An investigation of the conformity, feasibility, and expected clinical benefits of multiparametric MRI-guided dose painting radiotherapy in glioblastoma. Neurooncol Adv 2022;4:vdac134.

[40] Duprez F, De Neve W, De Gersem W, Coghe M, Madani I. Adaptive dose painting by numbers for head-and-neck cancer. Int J Radiat Oncol Biol Phys 2011;80:1045–55.

[41] Differding S, Sterpin E, Janssens G, Hanin FX, Lee JA, Grégoire V. Methodology for adaptive and robust FDG-PET escalated dose painting by numbers in head and neck tumors. Acta Oncol 2016;55:217–25.

[42] Rasmussen JH, Håkansson K, Vogelius IR, Aznar MC, Fischer BM, Friborg J, et al. Phase I trial of 18F-Fludeoxyglucose based radiation dose painting with concomitant cisplatin in head and neck cancer. Radiother Oncol 2016;120:76–80.

[43] Alber M, Thorwarth D. Multi-modality functional image guided dose escalation in the presence of uncertainties. Radiother Oncol 2014;111:354–9.

[44] Thorwarth D, Notohamiprodjo M, Zips D, Müller AC. Personalized precision radiotherapy by integration of multi-parametric functional and biological imaging in prostate cancer: A feasibility study. Z Med Phys 2017;27:21–30.

[45] Yan D, Chen S, Krauss DJ, Chen PY, Chinnaiyan P, Wilson GD. Tumor Voxel Dose-Response Matrix and Dose Prescription Function Derived Using (18)F-FDG PET/CT Images for Adaptive Dose Painting by Number. Int J Radiat Oncol Biol Phys 2019;104:207–18.

[46] Chen S, Qin A, Yan D. Dynamic Characteristics and Predictive Capability of Tumor Voxel Dose-Response Assessed Using (18)F-FDG PET/CT Imaging Feedback. Front Oncol 2022;12:876861.

[47] Wang C, Liu C, Chang Y, Lafata K, Cui Y, Zhang J, et al. Dose-Distribution-Driven PET Image-Based Outcome Prediction (DDD-PIOP): A Deep Learning Study for Oropharyngeal Cancer IMRT Application. Front Oncol 2020;10.

[48] Ji H, Lafata K, Mowery Y, Brizel D, Bertozzi AL, Yin F-F, et al. Post-radiotherapy PET image outcome prediction by deep learning under biological model guidance: a feasibility study of oropharyngeal cancer application. Front Oncol 2022;12.

[49] Lin NU, Lee EQ, Aoyama H, Barani IJ, Barboriak DP, Baumert BG, et al. Response assessment criteria for brain metastases: proposal from the RANO group. LancetOncol 2015;16:e270–8.

[50] Alexander BM, Brown PD, Ahluwalia MS, Aoyama H, Baumert BG, Chang SM, et al. Clinical trial design for local therapies for brain metastases: a guideline by the Response Assessment in Neuro-Oncology Brain Metastases working group. LancetOncol 2018;19:e33–42.

[51] Ocaña-Tienda B, Pérez-Beteta J, Romero-Rosales JA, Asenjo B, Ortiz de Mendivil A, Pérez Romasanta LA, et al. Volumetric analysis: Rethinking brain metastases response assessment. Neurooncol Adv 2024;6:vdad161.

[52] Håkansson K, Specht L, Aznar MC, Rasmussen JH, Bentzen SM, Vogelius IR. Prescribing and evaluating target dose in dose-painting treatment plans. Acta Oncol 2014;53:1251–6.